Published in final edited form as:
Nat Mater. ; 11(2): 120–125. doi:10.1038/nmat3169.

Synthesis of monolithic graphene – graphite integrated electronics

Jang-Ung Park[1,2,†,★], **SungWoo Nam**[3,†,★], **Mi-Sun Lee**[1], and **Charles M. Lieber**[2,3]

[1]School of Nano-Biotechnology and Chemical Engineering, School of Mechanical and Advanced Materials Engineering, Graphene Research Center, Ulsan National Institute of Science and Technology (UNIST), Ulsan Metropolitan City, 689-798, Republic of Korea

[2]Department of Chemistry and Chemical Biology, Harvard University, Cambridge, Massachusetts 02138, USA

[3]School of Engineering and Applied Sciences, Harvard University, Cambridge, Massachusetts 02138, USA

Abstract

Encoding electronic functionality into nanoscale elements during chemical synthesis has been extensively explored over the past decade as the key to developing integrated nanosystems[1] with functions defined by synthesis[2-6]. Graphene[7-12] has been recently explored as a two-dimensional nanoscale material, and has demonstrated simple device functions based on conventional top-down fabrication[13-20]. However, the synthetic approach to encoding electronic functionality and thus enabling an entire integrated graphene electronics in a chemical synthesis had not previously been demonstrated. Here we report an unconventional approach for the synthesis of monolithically-integrated electronic devices based on graphene and graphite. Spatial patterning of heterogeneous catalyst metals permits the selective growth of graphene and graphite, with controlled number of graphene layers. Graphene transistor arrays with graphitic electrodes and interconnects were formed from synthesis. These functional, all-carbon structures were transferrable onto a variety of substrates. The integrated transistor arrays were used to demonstrate real-time, multiplexed chemical sensing, and more significantly, multiple carbon layers of the graphene-graphite device components were vertically assembled to form a three-dimensional flexible structure which served as a top-gate transistor array. These results represent a substantial progress towards encoding electronic functionality via chemical synthesis and suggest future promise for one-step integration of graphene-graphite based electronics.

We demonstrate that differences in carbon solubility of metal catalyst films can be used to synthesize different thicknesses of graphene and graphite, and such catalyst films can be patterned to enable graphene and graphite patterns in localized and selected areas. For example, a Ni or Co film has relatively high solubility of carbon (> ~1.3 at.% at 1000 °C) and can produce graphite by segregation and precipitation of the carbon on the metal surface[18,19]. In comparison, Cu film has a negligible carbon solubility (< 0.0001 at.% at 1000 °C) and can generate ~1-3 graphene layers by carbon adsorption on Cu surface[17,21].

★Correspondence and requests for materials should be addressed to J.-U.P. (jangung@unist.ac.kr) and S.N. (nam@cmliris.harvard.edu). .
†J.-U. Park and S. Nam contributed equally.

Author Contributions J.-U.P., S.N. and C.M.L. designed the experiments. J.-U.P., S. N., and M.-S. L. performed the experiments. J.-U.P., S.N. and C.M.L. analyzed the data and wrote the paper.

Additional Information The authors declare no competing financial interests.

Supplementary information accompanies this paper on www.nature.com/naturematerials.

Fig. 1a illustrates the patterned catalyst films before the chemical vapor deposition (CVD) synthesis. Co and Ni were deposited with consonant and vowel alphabet structures, respectively, on a Cu film that was coated with a thin Ni protection top-layer against Cu oxidation. As temperature increased up to 1000°C during CVD synthesis, the deposited Co and Ni were locally diffused into the Cu layer to form alloys (Supplementary Fig. S1). After the synthesis and catalyst metal layer removal, the monolithic graphene-graphite structure was transferred to a 285 nm-thick SiO_2 substrate (Fig. 1b) (see Methods and Supplementary Information). Due to differences in reflection at the interface between air-graphene multilayers-SiO_2 depending on the number of graphene layers[22], the three parts (the consonant, vowel, and background) in Fig. 1b showed different colors and contrasts.

Raman spectra from these three different graphene-graphite regions (Fig. 1c) exhibited three characteristic bands (D: centered at ~1350 cm^{-1}, G: ~1590 cm^{-1}, 2D: ~2680 cm^{-1}) of graphene and graphite. The background region (synthesized from Cu) predominantly showed that the G band's intensity was comparable to 2D band's intensity, indicating 2 graphene layers[17,23]. We also observed the layer variations[24,25], and atomic force microscopy (AFM) measurements of step heights further confirmed the thickness of 2-4 layers (< 1.7 nm). Raman spectra obtained from the consonant area (Fig. 1c) showed that the G band's intensity was enhanced significantly and 2D band became non-symmetric and dispersive (broader) with slight blue shift due to interlayer binding, compared to the vowel region. This observation indicates that the thickness of the consonant part is thicker than the thickness of the vowel part[17,23], which was further confirmed by AFM measurement showing granular graphite grains with a thickness of ~40-190 nm in the consonant areas, and relatively thinner graphite with a thickness of ~2 ± 0.94 nm (~6-8 layers) in vowel parts. Phase separation of the Co-Cu alloy system occurs in the synthesis, and the consonant patterns contained both small graphite grains and few layer graphene parts synthesized together from Co-rich and Cu-rich phases, respectively. We also observed that sizes of the graphite grains increased with the thickness of the Co catalyst (Supplementary Fig. S2), and the film-like graphitic structures (thickness: ~300 ± 63 nm) with negligible areas of few layer graphene were synthesized when the Co catalyst was thick enough (thickness: > ~400 nm).

Fig. 1d shows two-dimensional maps of the G and 2D bands scanned on the synthesized area from the red-dashed square part in Fig. 1a. Both G and 2D bands mapping of the thick graphite region of the letter 'r' showed distinctive intensity contrast following the original catalyst pattern (Fig. 1d). In addition, mapping results showed that the graphite pattern was continuous and connected to the background 2-4 layer graphene, which clearly demonstrated monolithic synthesis of differing thicknesses. The cross-sectional transmission electron microscope (TEM) images (Supplementary Fig. S3a) further verified that the number of layers changes gradually at the interface between graphene and graphite with the uniform interlayer spacing. TEM characterization indicated that the graphite and graphene had formed continuous interface. Supplementary Fig. S3b and S3c represent hexagonal, electron diffraction patterns of the graphene and graphite from selected areas, respectively. Supplementary Fig. S4 shows energy dispersive X-ray analysis (EDAX) and X-ray photoelectron spectroscopy (XPS) analysis of the monolithic graphene-graphite transferred onto a Si wafer with a 285 nm-thick SiO_2 after the removal of catalyst metals (Cu, Ni, and Co). No characteristic peak of the metals was detected, which indicated that metal catalysts were completely removed by the etching process.

Electrical properties of graphene and graphite can be modulated by controlling the number of graphene layers (n). First, we show that conductivity or sheet resistance can be controlled by more than an order of magnitude, dependent on n. Films of graphene and graphite with differing n were synthesized using different metal catalyst films as previously described

(also see Methods and Supplementary Information). Fig. 2a shows the sheet resistance values of graphene and graphite measured using a four-point probe, as a function of *n*. The sheet resistance was reduced about 25 times (from 2,463±1,037 Ω/sq down to 98±46 Ω/sq), as *n* increased from ~2-4 to ~850 layers. The local variation of *n* influences the deviation of the sheet resistance. We also characterized the field-effect response of both 2-4 layer graphene and ~850 layer graphite (Supplementary Fig. S5). Current versus backgate characteristics showed much stronger modulation in 2-4 layer graphene, compared to negligible change in the thick graphite (~850 layers) due to stronger screening effect as the number of layers increases[26]. The low sheet resistance and field-effect response of graphite are advantageous for applications in conductive films or electrodes, in contrast to superior transconductance level of the 2-4 layer graphene which is appropriate for active channels of field-effect transistors (FETs).

The capability to modulate electronic properties through synthetic control of the graphite thickness provides a route to rationally designing and synthesizing large-scale electronics based entirely on carbon. The metal catalyst, Cu/Ni (700 nm/5 nm), was used to synthesize 2-4 layer graphene channels and the same combination with an additional Co (400 nm) was used to produce graphite electrodes which serve as the source (S) and drain (D) (Fig. 2b). This method enabled the fabrication of all-carbon based transistor arrays which were then transferred onto a 285 nm-thick SiO_2 on Si wafer for measurement of backgate response. Raman map (G band) of the monolithic graphene-graphite FET and AFM scan of interface between graphene channel and graphite electrode are demonstrated in Fig. 2c and Supplementary Fig. S6, respectively. S/D current (I_D) versus backgate bias (V_G) characterization of these FETs were performed at room temperature (Fig. 2d, black curve), which showed ambipolar behaviors consistent with the expected semimetallic characteristics of graphene[7,8,17,18] with a positive charge neutrality point of ~11 V. After thermal annealing step to remove resist residues, our monolithic graphene-graphite FET showed an improved hole (electron) mobility of ~1800 (1400) $cm^2/V{\cdot}s$ (Fig. 2d, red curve), calculated using a standard metal-oxide-semiconductor FET model. The evaporated Cu layer can cause dewetting of Cu on SiO_2/Si at the synthesis temperature, which can induce locally empty areas of the catalyst and defects in graphene causing reduced mobility values[16]. The optimization of defects in graphene[17,27] and growth and transfer conditions[24,25], and choosing substrates[28] with reduced roughness and chemical reactivity can further enhance the performance of our monolithic graphene-graphite FETs. Electrical properties of the interface between the graphene channel and graphite electrodes were compared to those of the interface between the graphene and Cr/Au metals (Cr: 2nm and Au 100 nm), as presented in Fig. 2e. I-V characteristics for both cases showed similar linear characteristics, at room temperature, without presenting any Schottky contact behaviors. Contact resistances of the graphene-metal (Cr/Au) junctions and the monolithic graphene-graphite were estimated at 300 K using transfer length method (Supplementary Fig. S7). Covalent graphite contacts to the graphene channels exhibit similar or slightly lower contact resistance (~700-900 $\Omega{\cdot}\mu m$) compared to that of Cr/Au (~1100 $\Omega{\cdot}\mu m$). In addition, our investigation showed that the graphite contacts with ~100 and ~300 nm in thicknesses do not exhibit significant difference in contact resistance. In addition to contact properties of graphite electrode to graphene channel, advantages of the graphite, compared to metals, lie in its superb mechanical flexibility. We observed that even when graphite electrodes were distorted up to strain of ~2 %, I-V characteristics remained the same (Fig. 2f).

The synthetic method facilitated the creation of a large-scale field-effect sensor arrays composed of monolithic graphene-graphite, which were transferred onto 285-nm SiO_2 / Si wafer. One block of the array contained nine of 2-4 layer graphene field-effect sensors with graphite single common source and independent drains. The sensor chip had four of these blocks composed of 36 sensor devices total, as illustrated in Fig. 3a. The graphite electrode

parts were covered with a 2 μm-thick SU8 passivation layer with openings around the 2-4 layer graphene channels. The current change measured while sweeping Ag/AgCl water-gate voltage at different pH solution is presented in Fig. 3b. The charge neutrality point shifted positively with increasing pH, and the pH sensitivity was ~17 mV/pH. These monolithic devices with the synthesized graphite electrodes showed similar sensitivity levels as the graphene sensors fabricated by standard lithography using the evaporated metal electrodes[29, 30]. However, compared to the previous reports using mechanically exfoliated graphene[29, 30], our regular sensor arrays with integrated geometries including interconnects obtained by synthesis demonstrated advantage for creating multiplexed sensor arrays. The water-gate response (Fig. 3b) exhibited ambipolar characteristics showing the possibility of complementary sensing at both p-type and n-type regimes. Statistic distributions of the normalized transconductance and charge neutrality point at pH 7 for the device array are shown in Fig. 3c and 3d. Gaussian fits of the two device parameters indicated center values of normalized transconductance and charge neutrality point of 540 ± 199 μS/V and -0.03 ± 0.038 V, respectively. Real-time multiplexed pH sensing using nine field-effect sensor array is demonstrated in Fig. 3e. Conductance increased (decreased) by switching solutions to higher (lower) pH in p-type regime (watergate potential: -0.1 V), and inverted responses were observed in n-type regime (0.3 V) as complementary sensing. The complementary sensing capability of graphene field-effect sensor is advantageous compared to other unipolar field-effect sensors[30] as it enables discrimination of possible electrical cross-talk and/or false-positive signals. Furthermore, the hydrophobic nature and high elastic modulus of the graphene/graphite enable the entire, monolithic arrays in a free-standing form to be floating on water sustainably (Fig. 3f). By transferring the floating arrays, the integrated device structures of monolithic graphene-graphite can be formed on various non-planar substrates. As examples, Fig. 3g demonstrates the monolithic devices wrapped on the outside surfaces of a thin cylindrical glass tube (outer diameter: ~1.5 mm), an eye contact lens (soft galyfilcon polymer), a glove finger (latex), a coin, and three different body areas of an insect (Odontolabis sarahssinorum specimen).

Flexible electronics represents an important application area that can take advantage of the monolithically integrated graphene-graphite devices. We demonstrate capabilities of assembling multiple layers of the synthesized graphene-graphite device components vertically as 3D integration, on plastic films (Fig. 4 and Supplementary Fig. S8). To realize this fabrication, the monolithically integrated graphene-graphite structures (2-4 layer graphene FET channel with ~850 layer graphite S/D and interconnects using the pattern shape similar in Fig. 3f) were transferred onto a polyether ether ketone (PEEK) film followed by deposition of SiO_2 dielectric layer. By assembling a graphitic (~6-8 graphene layers) topgate layer on the SiO_2, the flexible monolithic FET arrays were completed (see Methods and Supplementary Information). Fig. 4a and 4b show schematic illustrations of the device layouts and optical micrograph of the devices wrapped on a cylindrical glass support (radius of curvature: 1.2 cm). In addition to mechanical flexibility, optical transparency is another important characteristic of our monolithically integrated graphene-graphite circuits. As shown in the left inset of Fig. 4b, the underlying paper printed with a logo was clearly visible through the semitransparent top-gated devices that were positioned on top of the paper. Transmittance of single layer graphene is ~97 % at 550 nm wavelength, and decreases with higher n[24]. Therefore overall transparency of the monolithic devices can be adjusted by n of each device components. Although relatively less transparent graphite (~850 layers) was employed as S/D and interconnects (as shown in Fig. 4) to facilitate alignment of the topgate patterns using a conventional mask aligner, transmittance of final devices can be enhanced further with lower n.

Statistical distributions of the charge neutrality point and transconductance of the topgate FET arrays (average mobility: 675 cm^2/Vs) are provided in Fig. 4c, and these data fit

Gaussian profiles. Compared to the backgate FETs in Fig. 2, the charge neutrality point shifted close to zero, likely due to oxygen desorption from graphene in the SiO_2 evaporation step. Lastly, we studied mechanical flexibility of our monolithic graphene-graphite topgate FET devices. Fig. 4d presents current (I_D) versus topgate voltage (V_G) curves of the FET when the substrate was flat and bent (radius of curvature: 0.7 cm), which clearly showed no significant change in the electrical response (mobility values remained constant) resulting from bending to radii of curvature as small as 0.7 cm (estimated bending-induced strain: ~0.6 %). Electrical properties of the monolithic graphene-graphite devices can be nearly constant when applying maximum strain of ~4 %, demonstrating unique mechanical flexibility of our monolithic graphene-graphite integrated electronics (Supplementary Fig. S9).

Chemical synthesis of monolithic graphene-graphite electronics exhibits unique features compared to conventional Si-based fabrication and integrated electronics. From a materials synthesis perspective, our chemical synthesis of the entire graphene-graphite integrated electronics demonstrates the encoding of distinct electronic functionalities by synthetic control of graphene layers, and also simplifies intensive fabrication steps (e.g. lithography, ion-implantation, annealing, deposition, etching, etc.) necessary for conventional Si-based electronics. From a device perspective, monolithic graphene-graphite structure offers unique potential for flexible electronics/sensors. In comparison to the conventional integrated electronics which have mechanically fragile heterogeneous metal-semiconductor interfaces, our monolithic graphene-graphite devices demonstrate superb mechanical flexibility based on its monolithic interface that could be further explored up to the extent of the intrinsic mechanical properties of graphene/graphite[10]. Furthermore, high thermal conductivity (in-plane) and transparent electrical contacts of the monolithic geometries can be advantageous to enhancing the heat dissipation during device operations.

In conclusion, we have demonstrated chemical synthesis of monolithic graphene-graphite transistor arrays which can be transferred to various substrates and integrated to multilayer, 3D structures. We believe the capability to synthesize monolithic graphene-graphite integrated electronics provides a promising strategy towards flexible, wearable electronics and implantable biosensor devices, and also suggests substantial promise towards future graphene-based electronics in both two and three dimensions.

Methods

Spatially patterned, heterogeneous catalyst metal films were prepared by photolithography and thermal evaporation, and atmospheric CVD was carried out for the synthesis of the monolithic graphene-graphite structures. After the metal layers were removed in solution, the monolithic graphene-graphite structures were transferred onto Si substrate with 285 nm-thick SiO_2. For the fabrication of monolithic top-gate FETs, 400 nm-thick SiO_2 layer was evaporated as a gate dielectric and graphite film (6-8 graphene layers) was transferred and patterned as top-gate electrodes. Current versus back- and top-gate measurements were conducted with a probe station (model 12561B, Cascade Microtech) with a computer-controlled analog-to-digital converter (model 6030E, National Instruments) and a variable gain amplifier (1211 current preamplifier, DL Instruments, Inc.). Multichannel pH sensing was carried out with custom-designed variable gain amplifiers (multi-channel current preamplifier, SciMath Systems, LLC) and filtered using computer-based virtual lock-in amplifiers (multiplex 128-channel digital lock-in amplifier set-up kit, National Instruments).

Supplementary Material

Refer to Web version on PubMed Central for supplementary material.

Acknowledgments

We thank L. Wang for assistance on electrical measurements, Y. K. Kim for TEM characterization, and J. Cahoon and Q. Qing for helpful discussions. J.-U. P thanks UNIST for support through the 2010 Research Fund, and S.N. thanks the Samsung Scholarship. This research was supported by a research project of National Research Foundation of Korea (Grant number: 20110014111), and by a NIH Director's Pioneer Award (5DP1OD003900).

References

1. Lu W, Lieber CM. Nanoelectronics from the bottom up. Nature Mater. 2007; 6:841–850. [PubMed: 17972939]
2. Dai H. Carbon nanotubes: Synthesis, integration, and properties. Acc. Chem. Res. 2002; 35:1035–1044. [PubMed: 12484791]
3. Yang C, Zhong Z, Lieber CM. Encoding electronic properties by synthesis of axial modulation-doped silicon nanowires. Science. 2005; 310:1304–1307. [PubMed: 16311329]
4. Lauhon LJ, Gudiksen MS, Wang D, Lieber CM. Epitaxial core-shell and core-multishell nanowire heterostructures. Nature. 2002; 420:57–61. [PubMed: 12422212]
5. Kocabas C, Shim M, Rogers JA. Spatially selective guided growth of high-coverage arrays and random networks of single-walled carbon nanotubes and their integration into electronic devices. J. Am. Chem. Soc. 2006; 128:4540–4541. [PubMed: 16594668]
6. Zhou W, Ding L, Yang S, Liu J. Orthogonal orientation control of carbon nanotube growth. J. Am. Chem. Soc. 2010; 132:336–341. [PubMed: 20000705]
7. Novoselov KS, et al. Two-dimensional gas of massless dirac fermions in graphene. Nature. 2005; 438:197–200. [PubMed: 16281030]
8. Zhang Y, Tan Y, Stormer HL, Kim P. Experimental observation of the quantum Hall effect and Berry's phase in graphene. Nature. 2005; 438:201–204. [PubMed: 16281031]
9. Novoselov KS, et al. Electric field effect in atomically thin carbon films. Science. 2004; 306:666–669. [PubMed: 15499015]
10. Lee C, Wei X, Kysar JW, Hone J. Measurement of the elastic properties and intrinsic strength of monolayer graphene. Science. 2008; 321:385–388. [PubMed: 18635798]
11. Seol JH, et al. Two-dimensional phonon transport in supported graphene. Science. 2010; 328:213–216. [PubMed: 20378814]
12. Nair RR, et al. Fine structure constant defines visual transparency of graphene. Science. 2008; 320:1308–1308. [PubMed: 18388259]
13. Levendorf MP, Ruiz-Vargas CS, Garg S, Park J. Transfer-free batch fabrication of single layer graphene transistors. Nano Lett. 2009; 9:4479–4483. [PubMed: 19860406]
14. Kim KS, et al. Large-scale pattern growth of graphene films for stretchable transparent electrodes. Nature. 2009; 457:706–710. [PubMed: 19145232]
15. Jobst J, Waldmann D, Emtsev KV, Seyller Th. Weber HB. Transport properties of single-layer epitaxial graphene on 6H-SiC (0001). Mater. Sci. Forum. 2010; 645-648:637–641.
16. Mattevi C, Kim H, Chhowalla M. A review of chemical vapour deposition of graphene on copper. J. Mater. Chem. 2010; 21:3324–3334.
17. Li X, et al. Large-area synthesis of high-quality and uniform graphene films on copper foils. Science. 2009; 324:1312–1314. [PubMed: 19423775]
18. Reina A, et al. Large area, few-layer graphene films on arbitrary substrates by chemical vapor deposition. Nano Lett. 2009; 9:30–35. [PubMed: 19046078]
19. Jauregui LA, Cao H, Wu W, Yu Q, Chen YP. Electronic properties of grains and grain boundaries in graphene grown by chemical vapor deposition. Solid State Commun. 2011; 151:1100–1104.
20. Han MY, Ozyilmaz B, Zhang Y, Kim P. Energy band-gap engineering of graphene nanoribbons. Phys. Rev. Lett. 98:206805–2007. [PubMed: 17677729]
21. Li X, Cai W, Colombo L, Ruoff RS. Evolution of graphene growth on Ni and Cu by carbon isotope labeling. Nano Lett. 2009; 9:4268–4272. [PubMed: 19711970]
22. Blake P, et al. Making graphene visible. Appl. Phys. Lett. 2007; 91:063124.

23. Dresselhaus MS, Jorio A, Hofmann M, Dresselhaus G, Saito R. Perspectives on carbon nanotubes and graphene Raman spectroscopy. Nano Lett. 2010; 10:751–758. [PubMed: 20085345]

24. Bae S, et al. Roll-to-roll production of 30 inch graphene films for transparent electrodes. Nature Nanotech. 2010; 5:574–578.

25. Bhaviripudi S, Jia X, Dresselhaus MS, Kong J. Role of kinetic factors in chemical vapor deposition synthesis of uniform large area graphene using copper catalyst. Nano Lett. 2010; 10:4128–4133. [PubMed: 20812667]

26. Zhang Y, Small JP, Pontius WV, Kim P. Fabrication and electric-field-dependent transport measurements of mesoscopic graphite devices. Appl. Phys. Lett. 2005; 86:073104.

27. Yazyev OV, Louie SG. Electronic transport in polycrystalline graphene. Nature Mater. 2010; 9:806–809. [PubMed: 20729847]

28. Dean CR, et al. Boron nitride substrates for high-quality graphene electronics. Nature Nanotech. 2010; 5:722–726.

29. Ohno Y, Maehashi K, Yamashiro Y, Matsumoto K. Electrolyte-gated graphene field-effect transistors for detecting pH and protein adsorption. Nano Lett. 2009; 9:3318–3322. [PubMed: 19637913]

30. Cohen-Karni T, Qing Q, Li Q, Fang Y, Lieber CM. Graphene and nanowire transistors for cellular interfaces and electrical recording. Nano Lett. 2010; 10:1098–1102. [PubMed: 20136098]

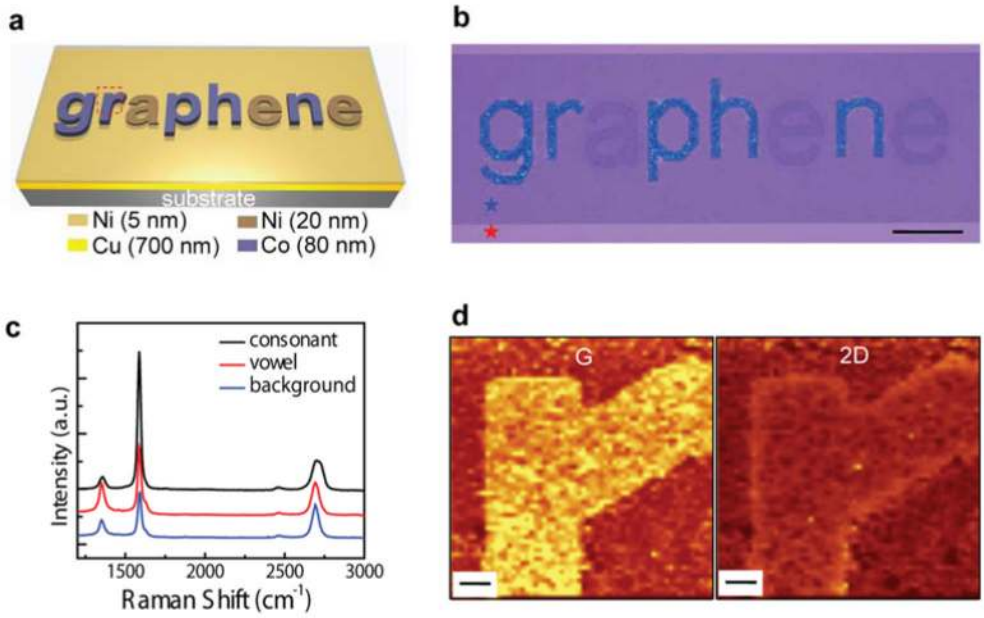

Figure 1. Synthesis of monolithic graphene-graphite structures using heterogeneously patterned catalyst metal films

a, Schematic illustration of alphabetic catalyst patterns. **b,** Optical micrograph of the graphene-graphite structures synthesized from the catalysts shown in Fig. 1a. The areas marked with red and blue stars represent SiO_2 and 2-4 layer graphene, respectively. Scale bar, 200 μm. **c,** Raman spectra from different regions (consonant, vowel, and background). **d,** Raman intensity maps of G (1537-1624 cm^{-1}) and 2D (2632-2778 cm^{-1}) bands in the region of alphabet pattern 'r'. Scale bars, 10 μm.

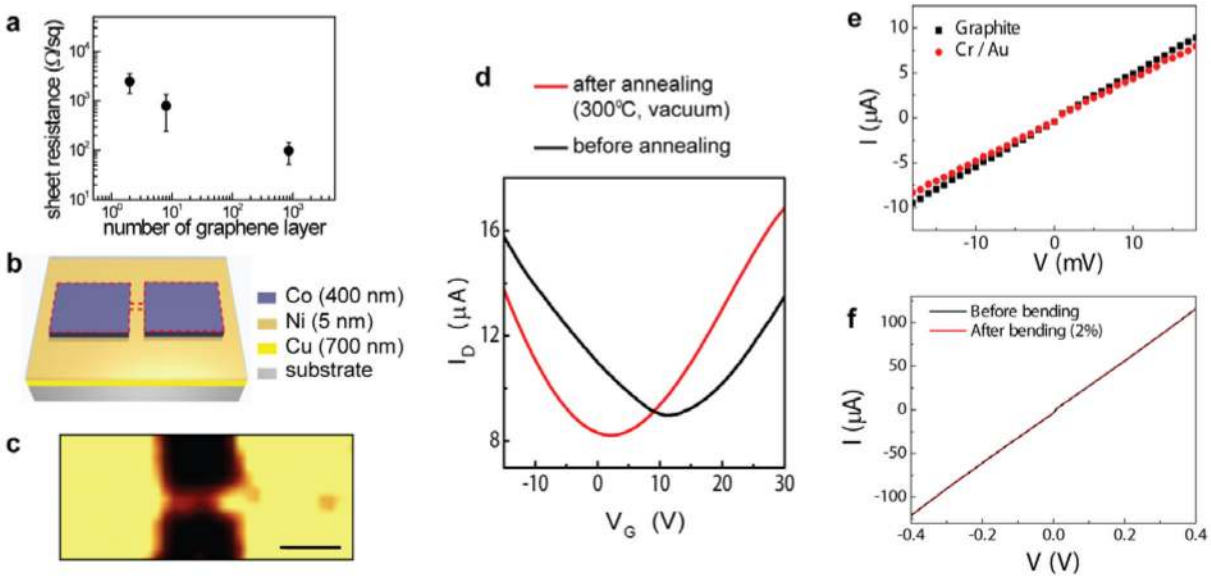

Figure 2. Synthesis and electrical characteristics of monolithic graphene-graphite backgate FETs

a, Sheet resistance as a function of the number of the graphene layers (*n*). The error bars represent one standard deviation. **b,** Schematic illustration of the catalyst pattern to synthesize the monolithic FET. Red-dashed lines indicate the masked area against O_2 plasma etching for device isolation after the CVD synthesis. **c,** Raman map (G band) of the graphene channel area with graphitic source/drain after the isolation step (channel width: 1 μm, length: 4 μm). Scale bar, 5 μm. **d,** I_D-V_G characteristics of monolithic graphene-graphite backgate FET (V_D: 0.1 V). **e**, Comparison of contact properties (i) between the monolithic graphene channel and graphite electrodes (black square) and (ii) between graphene and the Cr (2 nm) / Au (100 nm) electrodes evaporated on graphene (red), with the identical dimensions of electrode pads and the channel. **f**, Electrical characterization (I-V) of graphite electrode before and after elastic bending/distortion (strain of ~2%). Thickness of graphite electrodes in Fig. 2c-2f is ~300 ± 63 nm.

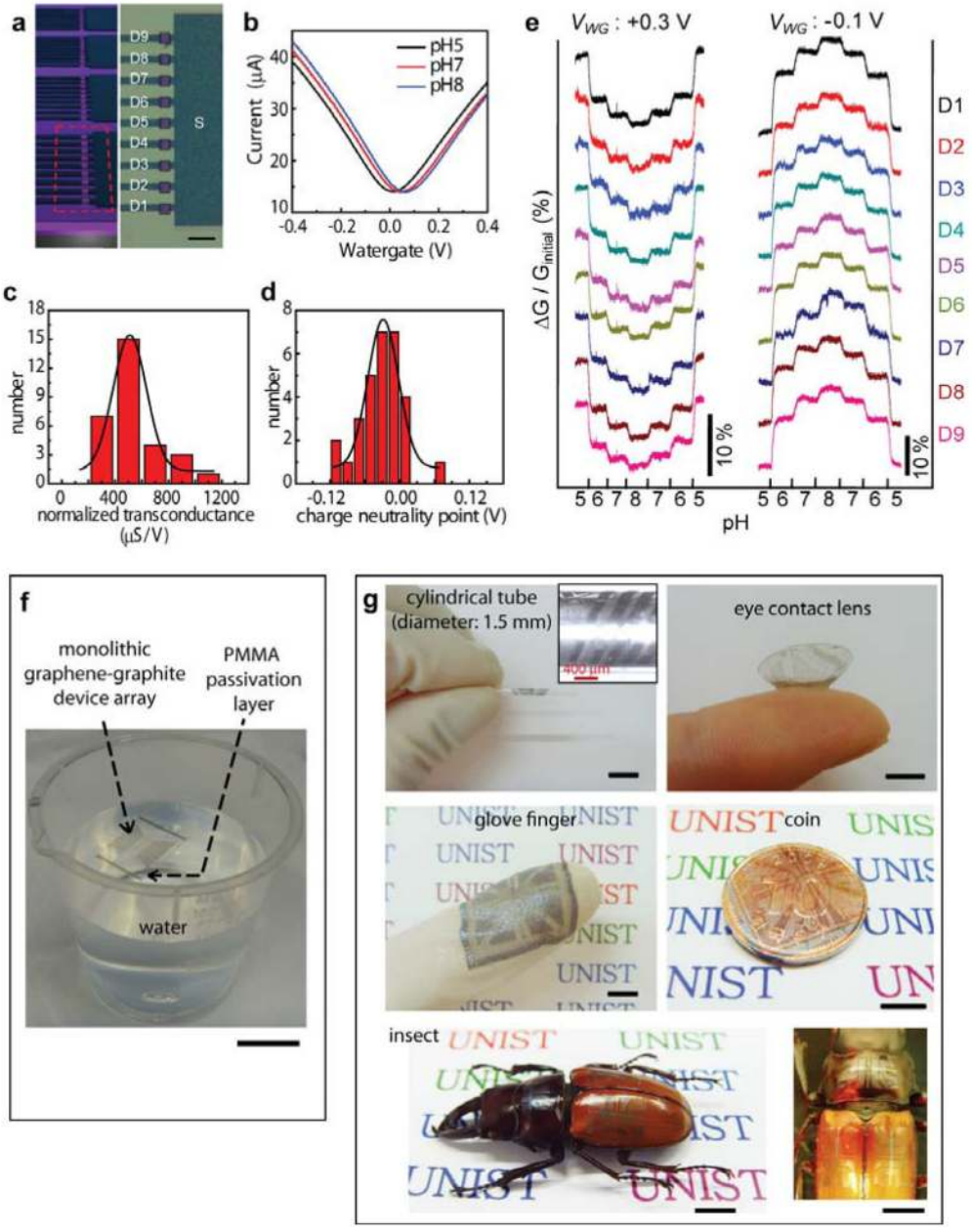

Figure 3. Real-time, multiplexed pH sensing using monolithic graphene field-effect sensor arrays with graphite electrodes

a, Schematic illustration (left panel) of the pH sensor array. 9 individual FETs compose one block, and the array has 4 blocks total. Optical micrograph of one block is shown in the right panel. Scale bar, 100 μm. **b,** Water-gate characterization at different pH levels. **c and d,** Statistic distributions of the normalized transconductance (in p-type) and charge neutrality point at pH 7. The transconductance in n-type also showed similar distributions. **e,** Complementary pH sensing using 9 monolithic field-effect sensors in both n-type (V_{WG}: +0.3 V) and p-type (V_{WG}: -0.1 V) regimes. V_{WG} is the water-gate potential and $G_{initial}$ is the conductance value at the starting condition (pH 5). **f,** Photograph of free-standing, monolithic graphene-graphite integrated sensor networks floating on water. Scale bar, 20 mm. Here, the array geometry is different from the form in **a** – **e**. **g,** Photographs of the

monolithic device structures transferred on various non-planar substrates such as a cylindrical glass tube (outer diameter: ~1.5 mm), eye contact lens (soft-type, galyfilcon), glove finger, coin, and the epidermis of an insect (odontolabis johani specimen). A magnified top-view image of the insect is shown on the right. Scale bars, 5 mm.

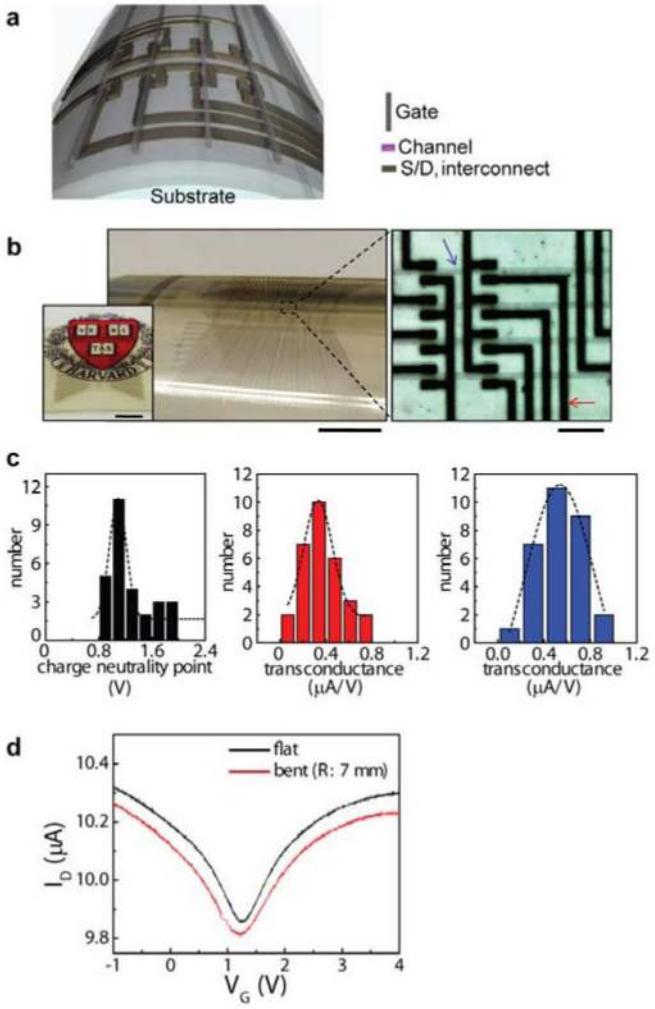

Figure 4. Flexible and semitransparent topgate monolithic graphene-graphite FET arrays

a, Schematic illustration of the device layout. **b,** Photograph (main panel) of the devices wrapped on a cylindrical glass (radius of curvature: 1.2 cm). The device rested on a paper printed with a logo, to demonstrate the semitransparent characteristics of the monolithic graphene-graphite devices (left inset). Scale bars, 4 mm. Optical micrograph of the topgate FET arrays (right image). Scale bar, 200 μm. The blue arrow presents the topgate line, and the red arrow indicates the S/D with interconnects. **c,** Statistic distributions of charge neutrality point (left panel) and transconductance at n-(center) and p- (right) type regimes. **d,** I_D-V_G curve of the topgate FET measured when the substrate is flat and bent (radius of curvature: 0.7 cm).